PHYSICS

Free-electron Ramsey-type interferometry for enhanced amplitude and phase imaging of nearfields

Tomer Bucher[1,2]†, Ron Ruimy[1,2]†, Shai Tsesses[1,3], Raphael Dahan[2], Guy Bartal[1], Giovanni Maria Vanacore[4], Ido Kaminer[1,2]*

The complex range of interactions between electrons and electromagnetic fields gave rise to countless scientific and technological advances. A prime example is photon-induced nearfield electron microscopy (PINEM), enabling the detection of confined electric fields in illuminated nanostructures with unprecedented spatial resolution. However, PINEM is limited by its dependence on strong fields, making it unsuitable for sensitive samples, and its inability to resolve complex phasor information. Here, we leverage the nonlinear, overconstrained nature of PINEM to present an algorithmic microscopy approach, achieving far superior nearfield imaging capabilities. Our algorithm relies on free-electron Ramsey-type interferometry to produce orders-of-magnitude improvement in sensitivity and ambiguity-immune nearfield phase reconstruction, both of which are optimal when the electron exhibits a fully quantum behavior. Our results demonstrate the potential of combining algorithmic approaches with state-of-the-art modalities in electron microscopy and may lead to various applications from imaging sensitive biological samples to performing full-field tomography of confined light.

INTRODUCTION

The interaction of electrons with static and dynamic electromagnetic fields lies at the center of numerous discoveries and applications. This interaction serves as the basic principle behind achieving atomic resolution (1, 2); it can result in important methods for characterizing the electronic (3) and magnetic (4) properties of materials, allows to promote and explore chemical processes (5), and helps in understanding many key cellular functions by visualizing macromolecular machines (6). In all abovementioned examples, the nontrivial and multifaceted nature of the interaction is essential.

A prime example for the interaction of electrons with electromagnetic fields is photon-induced nearfield electron microscopy (PINEM) (7–9). PINEM is an imaging technique relying on the inelastic scattering of free electrons from illuminated structures to reconstruct nearfield amplitudes on the nanoscale with potentially subnanometer (10) and subpicosecond (11) spatiotemporal resolutions. Beyond the time-resolved imaging of field dynamics (12), PINEM enables a plethora of additional abilities (13–18) such as detecting quantum emitter decoherence (19), reconstructing the quantum state of free electrons (20), generating attosecond electron bunches (21), and performing free-electron wavefront shaping (22, 23).

However, when used for imaging, PINEM extracts only the amplitude of the nearfield without any information about its phase and routinely neglects the inherent nonlinear connection between the nearfield and electron distributions (13, 14, 23). Therefore, it is clear that a large amount of latent information still exists in PINEM and can be exploited for the efficient electromagnetic investigation of nanoscale objects including weakly interacting ones. This

can only be achieved by integrating PINEM with another methodology, to increase the possible degrees of freedom for investigation.

In recent years, multiple techniques that rely on interferometry of electrons and light were developed to extend the abilities of PINEM. Notable examples include free-electron Ramsey-type phase control (20, 24), which relies on premodulating free electrons with a reference field while scanning over their relative phase. Inelastic electron holography (22) relies on premodulating free electrons with a reference field to generate an electron hologram of the sample field via the electron energy spectrum. Attosecond-pulse train techniques (21, 25) are based on premodulation of the free electrons followed by free propagation that shapes their charge distribution into a short attosecond trains. All these techniques enable phase-resolved measurement of nearfields due to their interferometric nature. However, these techniques primarily focused on the ability to perform phase-resolved (i.e., subcycle) measurements and did not consider the possibility of enhancing the imaging sensitivity.

In this work, we will focus on Ramsey-type free-electron interactions. Although sharing similar names, this phenomenon fundamentally differs from conventional, atom-based Ramsey interferometry schemes (26, 27), primarily because free electrons do not have a fixed set of internal degrees of freedom. Hence, the evolution of their quantum state under an applied ac electric field involves only a change in their total kinetic energy via photon absorption/emission (8), therefore applicable at arbitrary frequencies (28) and with a diverse range of samples.

It boasts a large, multidimensional parameter space, including the intensities and relative phase of the applied reference and sample fields, as well as the spectral and temporal properties of the fields and the free electron itself. Thus, integrating Ramsey-type control with PINEM is highly suitable for an algorithmic approach to optimize the extracted sample information, while potentially gaining added advantage from the quantum dynamics the electron undergoes by changing its kinetic energy.

[1]Andrew and Erna Viterbi Department of Electrical and Computer Engineering, Technion-Israel Institute of Technology, Haifa 3200003, Israel. [2]Solid State Institute, Technion-Israel Institute of Technology, Haifa 3200003, Israel. [3]Department of Physics and Research Laboratory of Electronics, Massachusetts Institute of Technology, Cambridge, MA 02139, USA. [4]Department of Material Science, University of Milano-Bicocca, Via Cozzi 55, 20121 Milano, Italy.
*Corresponding author. Email: kaminer@technion.ac.il
†These authors contributed equally to this work.

Here, we propose free-electron Ramsey-type imaging (FERI) to achieve enhanced imaging of both amplitude and phase of electromagnetic nearfields. We develop an algorithmic approach that optimizes the signal extracted from the overconstrained interaction, showing imaging with orders-of-magnitude less illumination power compared to conventional PINEM. We exemplify the approach by simulating FERI with illuminated gold nanospheres, which are potential markers in bioimaging (Fig. 1) (29, 30). FERI also enables ambiguity-immune phase-resolved nearfield imaging, requiring no prior knowledge regarding the sample, which we demonstrate by simulating the interaction of electrons with a hexagonal array of plasmonic vortices (23, 31).

Instead of relying on transverse electron coherence, as in electron holography methods (32, 33), FERI relies on temporal (longitudinal) coherence, greatly simplifying the electron source and optics, at the expense of more complex electromagnetic optics and addressing scheme. While our scheme is compatible with both quantum and classical, point-particle electrons, we provide analytical and numerical evidence that it performs optimally when the free electrons behave entirely as quantum particles. Thus, our approach promotes the use of light-driven electron microscopy in a plethora of platforms that could not have been investigated before and allows sensitive, low-dose characterization of materials, gaining advantage from the quantum nature of the free electron.

RESULTS

Imaging via premodulated electron pulses (FERI)

We begin by describing the interaction of electrons with nearfields —the theory that lies at the core of PINEM. The conventional PINEM theory usually considers an approximately monoenergetic electron of mean energy E_0 that interacts with a nearfield of central frequency ω (7–9, 11, 24). In addition, it is assumed that the electron energy spread σ_E, which is much smaller than E_0, is also smaller than the light quanta $\hbar\omega$, such that energy measurements distinguish between different number of absorbed/emitted quanta by the electron. This situation, commonly occurring in optical and near-infrared (IR) frequencies, is akin to requiring a quantum behavior of the electron. The majority of our analysis will focus on this case, but special attention will be given to the scenario $\sigma_E \gg \hbar\omega$ when analyzing the difference between a classical and quantum electron in FERI.

PINEM theory further assumes a paraxial electron with energy substantially higher compared to the light it interacts with ($E_0 \gg \hbar\omega$), such that the dispersion of the electron can be linearized. All the abovementioned approximations are typically satisfied under the operating conditions of ultrafast scanning and transmission electron microscopes as shown in previous works in the field (7–9, 11, 24, 34–38).

In this case, the Hamiltonian describing the interaction between the electromagnetic field and the electron is given by

$$H = E_0 - i\hbar v \partial_z + e v E_z(x, y, z)/\omega \qquad (1)$$

Here, v is the velocity of the electron, e is the fundamental charge, and z is the direction of propagation of the electron. According to this Hamiltonian, interactions between the electron matter wave and the electromagnetic wave result in a discrete energy exchange, such that the probability P_l to measure the electron with energy $E_0 + l\hbar\omega$ (with l being an integer) is given by $|J_l(2|g|)|^2$, where $g = \frac{e}{\hbar\omega}\int_{-\infty}^{\infty} dz E_z(x, y, z) e^{-\frac{iz\omega}{v}}$ is the dimensionless interaction constant. This parameter is thus the field's spatial Fourier component with wave vector ω/v. In general, $g = g(x, y)$ is a complex number and a function of the transverse coordinates (x, y). Because of the integral linear relation between $g(x, y)$ and the electric field, the amplitude and phase of g are proportional to those of the electric field along a specific line parallel to the z axis. One can recover both
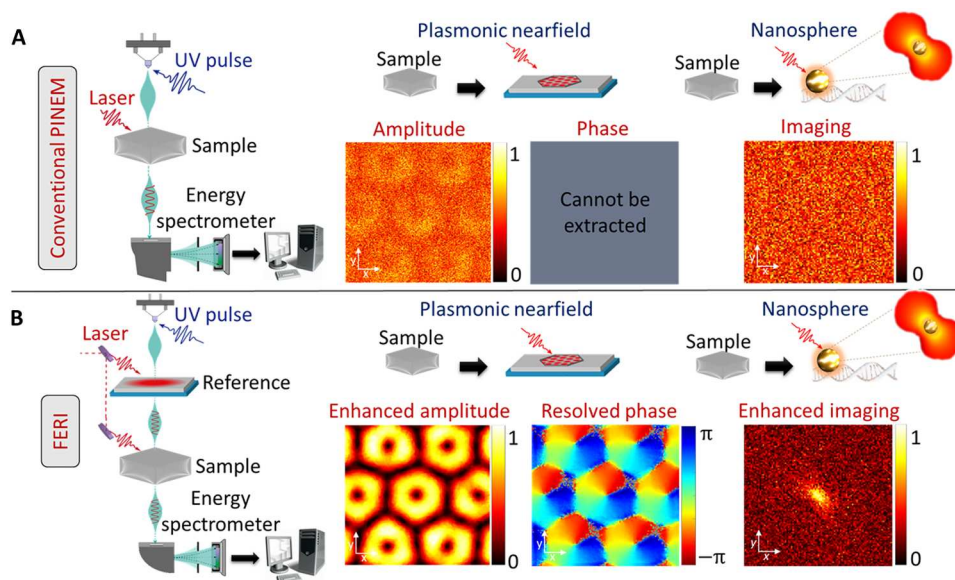

Fig. 1. FERI: Leveraging the complex free-electron interaction with confined fields for enhanced imaging. (**A**) Conventional photon-induced nearfield electron microscopy (PINEM) imaging versus (**B**) free-electron Ramsey-type imaging (FERI). Left: The interaction configuration. Middle: Reconstruction of the amplitude and phase of plasmonic nearfields with hexagonal symmetry, at a similar noise floor and laser intensity. Right: Reconstruction of the weak nearfield induced by a gold nanosphere, which can be used as a marker for bioimaging. UV, ultraviolet.

the amplitude and the phase of a specific Fourier component of the nearfield E_z $(x, y, k_z = \omega/v)$, which in the case of single nearfield mode can suffice to reconstruct the full field information such as in (31). In any case, currently, measuring $g(x, y)$ is the most that can be done in terms of nearfield imaging using the kind of interaction of PINEM. Using different sample tilts and electron velocities, one can in principle measure additional Fourier components of the nearfield. However, any energy-filtered spectrum measurement $\sum_{l \in L_{\text{filter}}} P_l$ can only extract information about the absolute value of the interaction constant, $|g|$.

This is the case in conventional measurement schemes (Fig. 1A), where one filters the signal over the entire gain side ($l > 0$) to extract the nearfield at the sample, given by the interaction constant $g_s(x, y)$. In this case, we can use identities of Bessel functions (39) to conclude (see section S2 in the Supplementary Materials for full derivation)

$$\text{Signal}(x, y) \propto \sum_{l=1}^{\infty} P_l(x, y) = \frac{1}{2}\{1 - J_0[2|g_s(x, y)|]^2\}$$
$$\approx |g_s(x, y)|^2 \qquad (2)$$

In the weak field regime ($g \ll 1$), the signal is directly proportional to the field intensity. The quadratic dependence requires relatively intense fields to collect enough signal, making conventional PINEM inappropriate for sensitive samples.

Because g is linear in the electric field, it can contain the superposition of two spatially separated fields, one acting as a reference and the other is the unknown sample field (22, 24, 25). Figure 1B presents the FERI scheme: It relies on the electron temporal (longitudinal) coherence to improve the detected PINEM signal at the sample by exploiting the additional coherent interaction with the reference field (with interaction constant g_r).

Figure 2 shows the working mechanics of the FERI scheme for phase reconstruction. By adding an additional subcycle phase delay $\Delta\phi$ between the reference and sample fields, it is possible to extract both the amplitude and phase of the sample field using energy filtering on the postinteraction electron. The relative phase delay overconstrains the measurement, as it adds up several images taken with different relative phases. The different raw measurements are sampled from different distributions, thus enhancing image contrast rather than just improving signal-to-noise ratio (as would happen in conventional PINEM if more images were to be added up).

In the particularly interesting case of samples characterized by weak fields, we can replace Eq. 2 using a modified formula that takes directly into account the presence of a reference field (see section S2 in the Supplementary Materials for full derivation)

$$\text{Signal}(x, y) \propto \sum_{l=1}^{\infty} P_l \approx \frac{1}{2}[1 - J_0(2|g_r|)^2] + 2J_0(2|g_r|)J_1(2|g_r|)$$
$$|g_s(x, y)| \cos[\angle g_s(x, y) - \Delta\phi] \qquad (3)$$

A critical point in Eq. 3 is the fact that the signal range of the measurement (in the limit of $|g_s| \ll 1$) scales as $|g_s|$, rather than of $|g_s^2|$. This fact alone results in substantial enhancement of the sensitivity of FERI when compared to conventional PINEM. Furthermore, using Eq. 3, we find the optimal amplitude of the reference field interaction constant ($|g_r^{\text{optimal}}|$) for any given case

where $|g_s| \ll 1$. It is given by the first positive solution to the equation $J_0(2x)^2 - J_2(2x)J_0(2x) - 2J_1(2x)^2 = 0$ (see section S2), which yields $|g_r^{\text{optimal}}| \approx 0.541$—a value well within reach of typical PINEM experiments (11). Using this optimal reference interaction, the signal range of the signal in a sample with maximal interaction $|g_s^m| \ll 1$ increases by the factor of $2J_1(2|g_r^{\text{optimal}}| J_0(2|g_r^{\text{optimal}}|)/|g_s^m| \sim 0.678/|g_s^m|$; (see section S2). It is noteworthy that more degrees of freedom arise from this analysis, such as scanning over different reference field interaction constants $|g_r|$ or by introducing and varying free-space propagation (see section S1).

This section discussed the limit of small $|g_s|$, which is the most interesting limit for sensitive samples, limited to weak illumination intensities. The analysis shows why and how FERI provides enhancement in this limit. In the following section, we describe our reconstruction algorithm, which applies for arbitrary values of $|g_s|$. The algorithm uses additional degrees of freedom of the interaction between electrons and nearfield to provide a general imaging enhancement, even in the limits of relatively large $|g_s|$. The regime of small $|g_s|$ shows the maximum enhancement and is also the most relevant.

Enhanced and phased-resolved nearfield imaging

PINEM applications for field imaging have thus far used energy-filtered transmission electron microscopy (EFTEM), filtering electrons over a certain range, only extracting part of the spatial information of the field. The signal in such cases is linear in the field intensity. Once we perform a premodulating interaction, the field at the sample can interfere with different interaction orders l, and by energy filtering the electrons, the nonlinearity of the relation between field and electron distributions provides a substantial additional information. The general energy-filtered electron distribution measurement can be described as $M = \sum_{l \in L_{\text{filter}}} P_l = \sum_{l \in L_{\text{filter}}} |J_l(2|g_{\text{total}}|)|^2$, with $g_{\text{total}} = g_r + g_s$ and L_{filter} being the range of filtered energies. The measured signal for each relative subcycle delay $\Delta\phi$ and each transverse sample coordinate x, y is

$$M[x, y, \Delta\phi, L_{\text{filter}}, |g_s(x,y)|, \angle g_s(x,y)]$$
$$= \sum_{l \in L_{\text{filter}}} |J_l\{2\sqrt{|g_r|^2 + |g_s(x,y)|^2 + 2|g_r||g_s(x,y)|\cos[\angle g_s(x,y) - \Delta\phi]}\}|^2 \qquad (4)$$

The measurement model expression is ambiguous, i.e., multiple values of $\{|g_s|, \angle g_s\}$ can output the same value of energy-filtered electron distribution measurement, denoted as $Y(x, y, \Delta\phi, L_{\text{filter}})$. To remove this ambiguity and extract the correct field g_s, the optimization procedure (Fig. 3) scans over the relative phase between the reference field and sample field. Although not used here, additional information can also be gained by scanning over the filtered energy range. By using maximum likelihood estimation (MLE) with the measurement model M, the reconstruction of the amplitude and phase of the sample is performed per $\{x, y\}$ coordinate by minimizing the following expression

$$\underset{|g_s(x,y)|, \angle g_s(x,y)}{\text{argmin}} \sum_{\Delta\phi, L_{\text{filter}}} |Y(x, y, \Delta\phi, L_{\text{filter}}) - M[x, y, \Delta\phi, L_{\text{filter}}, |g_s(x,y)|, \angle g_s(x,y)]|^2 \qquad (5)$$

The measurement scheme can also be more generally performed with scanning TEM electron energy loss spectroscopy (STEM-EELS), where the entire electron energy spectrum is measured per
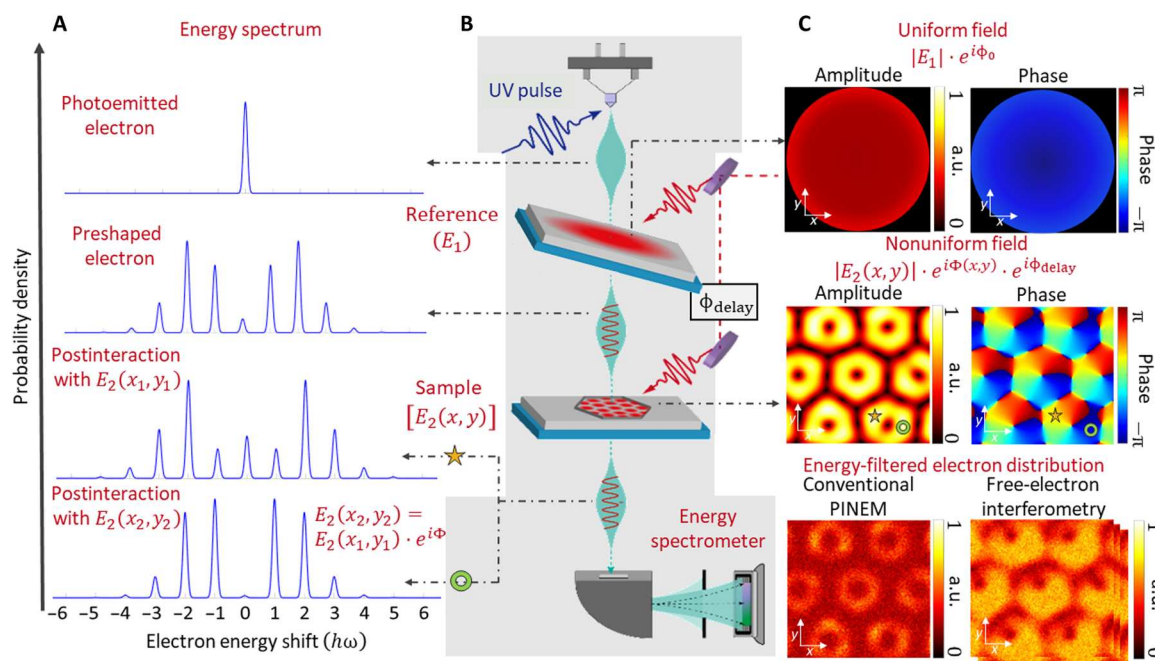
Fig. 2. FERI measurement scheme. A free electron in an ultrafast transmission electron microscope is premodulated via an interaction with a reference field. The premodulated electron probes the sample field, which is delayed by less than an optical cycle relative to the reference field. The complex value of the field (both amplitude and phase) is probed by measuring the distribution of energy-filtered electrons. (**A**) Evolution of the electron spectral probability density (SPD) as it propagates through the system, in given coordinates (x, y). The bottom two SPD showcase how the phase information of the field and the nonlinear connection between its value and the electron distribution changes the measured signal at different locations. (**B**) Illustration of the free-electron Ramsey-type imaging (FERI) scheme. (**C**) Top: The reference field, consisting of a uniform amplitude and phase. Middle: The sample field (amplitude and phase). Bottom: Energy-filtered electron distribution measurements for conventional photon-induced nearfield electron microscopy (PINEM) (left) and FERI (right). From the latter, both the amplitude and phase can be reconstructed. a.u., arbitrary units.

point, as opposed to EFTEM, which measures the entire spatial distribution for a given electron energy range. Performing STEM-EELS (which acts similarly to performing EFTEM while scanning over the energy filtered range) may improve the field reconstruction but requires longer data acquisition times.

As the MLE expression in Eq. 5 is not convex, gradient descent can converge to a local minimum. To solve this issue, the minimization method used is summation of MLE heatmaps for all relative phases (and energy filters, if relevant), while choosing the minimum value of the joint MLE heatmap. This approach guarantees convergence to the global minima, as exemplified in Fig. 3 for an arbitrary phase profile and for plasmonic optical vortices (*31*) (simulated using the Huygens principle method (*40*) as described in section S4). After reconstructing $|g_s(x, y)|$, $\angle g_s(x, y)$ for every coordinate $\{x, y\}$, we further use a denoising convolutional neural network (DnCNN) (*41*) for further signal improvement, making use of natural image prior knowledge. The DnCNN uses the concept of residual learning, making it possible to denoise arbitrary confined field images.

Many phase retrieval methods require solving optimization problems for the transverse plane, but they often encounter ambiguities such as global phase shifts, conjugate inversions, and spatial shifts. More complex ambiguities stem from the nonconvexity of the optimization problem (*42, 43*). In our example of plasmonic optical vortices, determining the rotation direction of the vortex presents an ambiguity. However, FERI prevents these ambiguities because its optimization is performed per pixel instead of on the

entire transverse plane, while using combinations of several MLE heatmaps.

We exemplify this procedure on plasmonic standing waves with hexagonal geometry (Fig. 2C), which can be measured in PINEM experiments (*23*). We choose this example as it presents a physical field with varying field strengths and oscillating phase and define the $|g_s|$ as the average $|g|$ over the entire image. We measure the reconstruction fidelity relative to the ground truth using the structural similarity index measure (SSIM) (*44*) and use it to compare our FERI scheme with conventional PINEM. The SSIM comparison shows an improvement by almost two orders of magnitude for the minimal interaction strength necessary for the reconstruction (Fig. 4A).

The signal in our simulation is the empirical probability of the electron to pass a given energy filter, which then gets an additional white Gaussian noise with SD σ_N to take into account the many sources of potential noises inside an electron microscope. We derive the minimal interaction strength needed to successfully image a given σ_N. For conventional PINEM, it follows $|g_{min}^{PINEM}| \approx 0.315\sqrt{\sigma_N}$; when with FERI, $|g_{min}^{FERI}| \approx 0.15\sigma_N$; and when introducing DnCNN, $|g_{min}^{DnCNN-FERI}| \approx 0.075\sigma_N$. The parameters were extracted from a linear fit to the data in Fig. 4A and can vary by the choice of SSIM threshold. That said, the difference in scaling follows an approximate analytical relation for the minimal
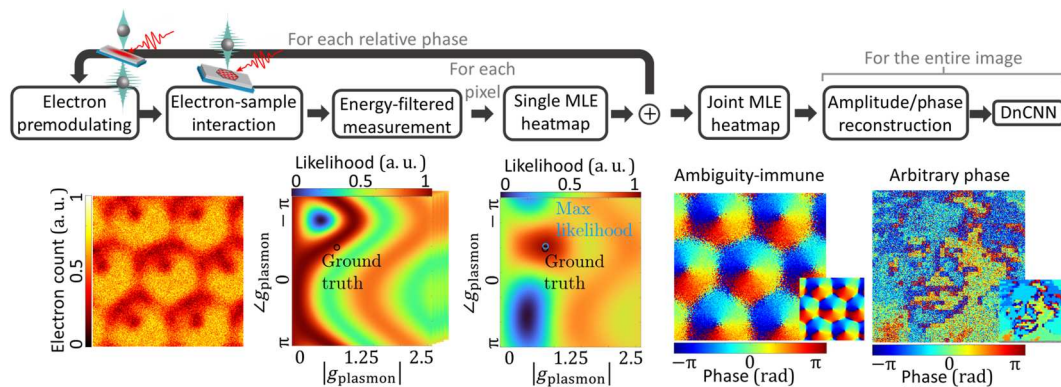
Fig. 3. Phase-resolved optimization. Block scheme (top) and visualization (bottom) of the optimization process. The free electrons are premodulated by a reference field before they probe the sample field and are energy filtered to produce electron distribution measurements (bottom row, first from the left). For each transverse pixel, several maximum likelihood estimation (MLE) heatmaps are generated, for different relative phases between the reference and signal fields (bottom row, second from the left). The summed joint MLE heatmap (bottom row, third from the left) enables the accurate estimation of the amplitude and phase for each pixel. Last, a denoising convolutional neural network (DnCNN) enhances the amplitude/phase reconstruction. To the right are two phase-reconstruction examples: plasmonic optical vortices and an arbitrary phase (a pixelated Einstein portrait), with the corresponding ground truth images in insets. The average $g_s(x, y)$ used for these examples is ~1 and $g_r \approx$ 0.541. The ground truth of the absolute value of $g_{plasmon}$ presented in this figure is ~1; however, the algorithm is completely general for arbitrary parameters.

interaction strength

$$|g_{min}^{PINEM}| \approx \frac{1}{\sqrt{2}} \cdot \sqrt{|g_{min}^{FERI}|} \approx \sqrt{2} \cdot \sqrt{|g_{min}^{DnCNN-FERI}|} \quad (6)$$

This square relation between PINEM and FERI is consistent with Eqs. 2 and 3, while the factor of $\frac{1}{\sqrt{2}}$ relates to the signal range derived in section S2. We can see here that by using further algorithmic improvements, such as DnCNN, we can improve the multiplying factor to the minimal interaction strength.

Such improvements in sensitivity and low-dose operation are especially important when attempting to image sensitive materials or objects weakly interacting with the applied electromagnetic field. To quantify these prospects, we analyze the FERI-based enhancement of PINEM signals from gold nanospheres, which can be used as part of markers in bioimaging, sequencing, and diagnosis (29, 45–48). Detection of nanospheres induced by weak laser fluence can be used in DNA labeling to enhance or replace fluorescence markers (49–51). We envision nanospheres that are attached to DNA molecules (as illustrated in Fig. 4B) to help visualize, detect, and label DNA inside light-driven electron microscopes.

By using laser intensities that are conventional in such experiments and identical noise floor (14), we demonstrate a quantitative advantage of FERI over PINEM. For the same parameters in which conventional PINEM can detect gold nanospheres with a radius of 30 nm, FERI can detect nanosphere with radius of 14 nm (Fig. 4B). From the perspective of power efficiency, this corresponds to 100-fold reduction in the necessary laser fluence for the detection of a nanosphere with a given size. For details regarding the nanosphere simulation [based on (52)] and the parameters used to generate Fig. 4B, we direct the reader to section S5.

The quantum nature of free electrons and its effect on FERI

Up until now, we only considered the electron as a quantum particle, i.e., having energy spread σ_E smaller than the light energy quantum $\hbar\omega$. In the limit $g_s \ll g_r \ll 1$, Eq. 3 directly reproduces the result of using the quantum coherence of a free electron for sensing applications (53), up to a redefinition of the measured

signal. In the following section, we consider the case of an electron as a classical particle, i.e., that its energy spread σ_E is larger than the light energy quantum $\hbar\omega$. One might initially think that FERI would not be effective under these conditions, as it may appear impossible to resolve the PINEM peaks, for example, in the case of mid-IR PINEM (12). However, even this classical electron should gain substantial improvement in sensitivity by using our scheme. The reason is that the electron-mediated interference term between the fields in Eq. 3 relies solely on the coherence of the fields, regardless of the electron energy spread. The information is then stored in the classical analog of the quantum phase—the electron velocity.

A classical, point particle electron can be directly defined by the limit $\sigma_E \gg \hbar\omega$, and it produces a conventional PINEM signal only when $g\hbar\omega > \sigma_E$, requiring a substantial investment of energy ($g \gg 1$). This is a direct result of the inability to completely separate the initial and light-induced electron spectral probability density or more generally—to resolve specific PINEM orders. Although FERI should improve sensitivity, the interference term within the PINEM signal, which is responsible for this improvement, is reduced by the factor $\text{erf}\left(\frac{\hbar\omega}{\sigma_E}\right)$ (53). The direct consequence of this reduced sensitivity is a rescaling of interaction constants, increasing both the optimal reference interaction constant and the required sample interaction constant by the same factor, $\text{erf}\left(\frac{\hbar\omega}{\sigma_E}\right)$.

In the classical regime, some electrons always pass the energy filter due to the erf function, contributing a constant background signal. In this case, even in the limit of shot-noise–limited measurements, FERI introduces an additional enhancement exemplified in the linear regime ($g_r, g_s \ll 1$) by

$$\delta g_s^{classical} = \frac{1}{2\sqrt{N}} \sqrt{\frac{a}{b^2} \cdot \frac{1}{g_{total}} + \frac{1}{b}}, a = \frac{1}{2} - \frac{1}{2}\text{erf}\left(\frac{E_f}{\sqrt{2}\sigma_E}\right), b$$

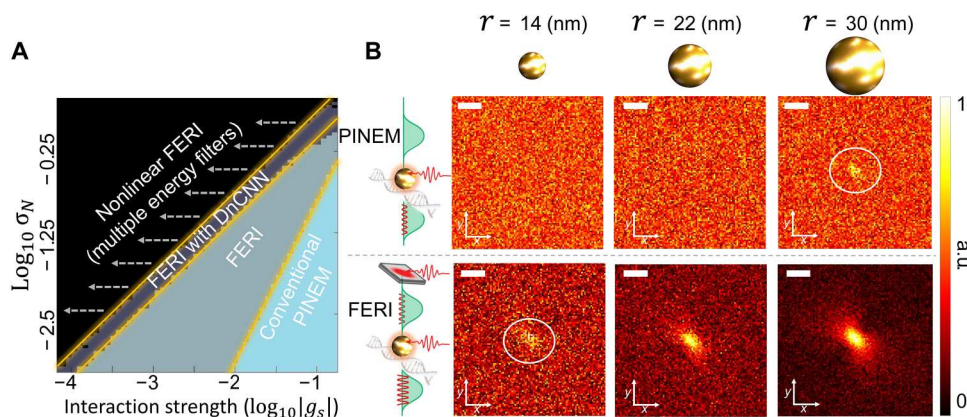$$= \frac{\hbar\omega}{\sqrt{2\pi}\sigma_E} \cdot e^{-\frac{E_f^2}{2\sigma_E^2}} \quad (7)$$

Fig. 4. Enhanced nearfield imaging using FERI. (**A**) Successful amplitude reconstruction for the plasmonic field [structural similarity index measure (SSIM) > 0.4] for conventional photon-induced nearfield electron microscopy (PINEM) (turquoise), free-electron Ramsey-type imaging (FERI) (light gray), and with an added denoising convolutional neural network (DnCNN) (dark gray). Additional information, such as that gained by using several energy filtering ranges, increases sensitivity even further. $|g_s|$ is defined as the average interaction strength over the image. (**B**) Imaging of laser-excited gold nanospheres for different sphere radii. The figure shows the reconstructed $|g_s|$ using (top) conventional PINEM imaging and (bottom) FERI. We considered the same white noise with $\sigma_N = 0.27$ and same excitation intensity in all panels. Scale bar, 15 nm. The spheres could be envisioned as markers for biological samples, e.g., single DNA strings. See section S5 for full details regarding the simulation details.

where E_f is the energy filter with respect to the electron's initial mean energy E_0 (see section S6).

Equation 7 shows that the estimation error is decreasing with respect to g_r, because of the background signal, making FERI particularly useful in the case where the zero-loss peak spread is wider than the photon energy $\hbar\omega$, for example, in the mid-IR and Terahertz regimes.

DISCUSSION

The enhancement of FERI fundamentally arises from the longitudinal (temporal) coherence of the electron (either quantum or classical). It is intriguing to compare this approach with more conventional methods that rely on transverse coherence, such as electron holography (*32*), which were recently studied with ultrafast electron microscopes (*22, 33, 54*). Using longitudinal coherence avoids limitations due to electron beam quality and could enable operation with simpler, higher-flux electron sources. Because longitudinal electron coherence represents a robust parameter, FERI measurements can even be performed with slower electrons in scanning electron microscopes (*55*). Thus, FERI seems to be a route that is easier to follow.

Possible extensions of our work can explore increasing the spatial resolution to the atomic scale, using sample tilt to perform full-field tomography, and operate at low (<10 K) temperatures using liquid helium cryo-holders (*56*), providing a unique probe for cold condensed matter physics. The sensitivity enhancement showed in this work also makes FERI a promising approach to demonstrate enhanced cathodoluminescence (*57*) as well as free-electron–bound-electron resonant interaction (*58*), which had not been realized experimentally so far, due to its intrinsically weak interaction.

As a final remark, we note that 1 month after the submission of the first version of this work, a paper by the Baum group (*59*) demonstrated the first phase-resolved interferometric nearfield imaging inside a transmission electron microscope. In parallel with the submission of the first version of this work, experiments by the Ropers group and by our group (*60, 61*), also demonstrated phase-resolved interferometric nearfield imaging inside transmission electron microscopes. These experiments show the increasing interest and rapid development in Ramsey-type interferometric schemes in the field. Relative to these works, our current manuscript is unique in proposing the concept of coherent amplification using free electrons and in providing the algorithm for its implementation. Bucher *et al.* (*60*) are the first to demonstrate this concept experimentally. The approach we presented here can be directly applied in other interferometric experiments, such as (*59, 61*).

Supplementary Materials

This PDF file includes:
Sections S1 to S6
Fig. S1

REFERENCES AND NOTES

1. K. W. Urban, Studying atomic structures by aberration-corrected transmission electron microscopy. *Science* **321**, 506–510 (2008).
2. A. Polman, M. Kociak, F. J. García de Abajo, Electron-beam spectroscopy for nanophotonics. *Nat. Mater.* **18**, 1158–1171 (2019).
3. H. J. Leamy, Charge collection scanning electron microscopy. *J. Appl. Phys.* **53**, R51–R80 (1982).
4. X. Fu, S. D. Pollard, B. Chen, B. Yoo, H. Yang, Y. Zhu, Optical manipulation of magnetic vortices visualized in situ by Lorentz electron microscopy. *Sci. Adv.* **4**, eaat3077 (2018).
5. J. M. Thomas, O. Terasaki, The electron microscope is an indispensable instrument for the characterisation of catalysts. *Topics Catal.* **21**, 155–159 (2002).
6. W. Baumeister, A. C. Steven, Macromolecular electron microscopy in the era of structural genomics. *Trends Biochem. Sci.* **25**, 624–631 (2000).
7. B. Barwick, D. J. Flannigan, A. H. Zewail, Photon-induced near-field electron microscopy. *Nature* **462**, 902–906 (2009).
8. F. J. García De Abajo, A. Asenjo-Garcia, M. Kociak, Multiphoton absorption and emission by interaction of swift electrons with evanescent light fields. *Nano Lett.* **10**, 1859–1863 (2010).
9. S. T. Park, M. Lin, A. H. Zewail, Photon-induced near-field electron microscopy (PINEM): Theoretical and experimental. *New J. Phys.* **12**, 123028 (2010).
10. A. H. Zewail, Four-dimensional electron microscopy. *Science* **328**, 187–193 (2010).

11. A. Feist, K. E. Echternkamp, J. Schauss, S. V. Yalunin, S. Schäfer, C. Ropers, Quantum coherent optical phase modulation in an ultrafast transmission electron microscope. *Nature* **521**, 200–203 (2015).

12. Y. Kurman, R. Dahan, H. H. Sheinfux, K. Wang, M. Yannai, Y. Adiv, O. Reinhardt, L. H. G. Tizei, S. Y. Woo, J. Li, J. H. Edgar, M. Kociak, F. H. L. Koppens, I. Kaminer, Spatiotemporal imaging of 2D polariton wave packet dynamics using free electrons. *Science* **372**, 1181–1186 (2021).

13. O. Kfir, H. Lourenço-Martins, G. Storeck, M. Sivis, T. R. Harvey, T. J. Kippenberg, A. Feist, C. Ropers, Controlling free electrons with optical whispering-gallery modes. *Nature* **582**, 46–49 (2020).

14. K. Wang, R. Dahan, M. Shentcis, Y. Kauffmann, A. Ben Hayun, O. Reinhardt, S. Tsesses, I. Kaminer, Coherent interaction between free electrons and a photonic cavity. *Nature* **582**, 50–54 (2020).

15. G. M. Vanacore, G. Berruto, I. Madan, E. Pomarico, P. Biagioni, R. J. Lamb, D. McGrouther, O. Reinhardt, I. Kaminer, B. Barwick, H. Larocque, V. Grillo, E. Karimi, F. J. García de Abajo, F. Carbone, Ultrafast generation and control of an electron vortex beam via chiral plasmonic near fields. *Nat. Mater.* **18**, 573–579 (2019).

16. T. T. A. Lummen, R. J. Lamb, G. Berruto, T. Lagrange, L. Dal Negro, F. J. García De Abajo, D. McGrouther, B. Barwick, F. Carbone, Imaging and controlling plasmonic interference fields at buried interfaces. *Nat. Commun.* **7**, 13156 (2016).

17. L. Piazza, T. T. A. Lummen, E. Quiñonez, Y. Murooka, B. W. Reed, B. Barwick, F. Carbone, Simultaneous observation of the quantization and the interference pattern of a plasmonic near-field. *Nat. Commun.* **6**, 6407 (2015).

18. Y. Adiv, K. Wang, R. Dahan, P. Broaddus, Y. Miao, D. Black, K. Leedle, R. L. Byer, O. Solgaard, R. J. England, I. Kaminer, Quantum nature of dielectric laser accelerators. *Phys. Rev. X* **11**, 041042 (2021).

19. R. Ruimy, A. Gorlach, C. Mechel, N. Rivera, I. Kaminer, Toward atomic-resolution quantum measurements with coherently shaped free electrons. *Phys. Rev. Lett.* **126**, 233403 (2021).

20. K. E. Priebe, C. Rathje, S. V. Yalunin, T. Hohage, A. Feist, S. Schäfer, C. Ropers, Attosecond electron pulse trains and quantum state reconstruction in ultrafast transmission electron microscopy. *Nat. Photonics* **11**, 793–797 (2017).

21. Y. Morimoto, P. Baum, Diffraction and microscopy with attosecond electron pulse trains. *Nat. Phys.* **14**, 252–256 (2018).

22. I. Madan, G. M. Vanacore, E. Pomarico, G. Berruto, R. J. Lamb, D. McGrouther, T. T. A. Lummen, T. Latychevskaia, F. J. García de Abajo, F. Carbone, Holographic imaging of electromagnetic fields via electron-light quantum interference. *Sci. Adv.* **5**, eaav8358 (2019).

23. S. Tsesses, R. Dahan, K. Wang, T. Bucher, K. Cohen, O. Reinhardt, G. Bartal, I. Kaminer, Tunable photon-induced spatial modulation of free electrons. *Nat. Mater.* **22**, 345–352 (2023).

24. K. E. Echternkamp, A. Feist, S. Schäfer, C. Ropers, Ramsey-type phase control of free-electron beams. *Nat. Phys.* **12**, 1000–1004 (2016).

25. A. Ryabov, J. W. Thurner, D. Nabben, M. V. Tsarev, P. Baum, Attosecond metrology in a continuous-beam transmission electron microscope. *Sci. Adv.* **6**, eabb1393 (2022).

26. N. Ramsey, *Molecular Beams* (Oxford Univ. Press, 1956), vol. 20.

27. P. Bertet, S. Osnaghi, A. Rauschenbeutel, G. Nogues, A. Auffeves, M. Brune, J. M. Raimond, S. Haroche, A complementary experiment with an interferometer at the quantum-classical boundary. *Nature* **411**, 166–170 (2001).

28. O. Kfir, V. Di Giulio, F. J. G. de Abajo, C. Ropers, Optical coherence transfer mediated by free electrons. *Sci. Adv.* **7**, eabf6380 (2021).

29. R. A. Sperling, P. R. Gil, F. Zhang, M. Zanella, W. J. Parak, Biological applications of gold nanoparticles. *Chem. Soc. Rev.* **37**, 1896–1908 (2008).

30. M. De, P. S. Ghosh, V. M. Rotello, Applications of nanoparticles in biology. *Adv. Mater.* **20**, 4225–4241 (2008).

31. S. Tsesses, K. Cohen, E. Ostrovsky, B. Gjonaj, G. Bartal, Spin-orbit interaction of light in plasmonic lattices. *Nano Lett.* **19**, 4010–4016 (2019).

32. P. Simon, H. Lichte, P. Formanek, M. Lehmann, R. Huhle, W. Carrillo-Cabrera, A. Harscher, H. Ehrlich, Electron holography of biological samples. *Micron* **39**, 229–256 (2008).

33. J. H. Gaida, H. Lourenço-Martins, S. V. Yalunin, A. Feist, M. Sivis, T. Hohage, J. García de Abajo, C. Ropers, Lorentz microscopy of optical fields. *Res. Sq.* 10.21203/rs.3.rs-2150760/v1, (2022).

34. O. Reinhardt, I. Kaminer, Theory of shaping electron wavepackets with light. *ACS Photonics* **7**, 2859–2870 (2020).

35. S. T. Park, A. H. Zewail, Relativistic effects in photon-induced near field electron microscopy. *J. Phys. Chem. A* **116**, 11128–11133 (2012).

36. S. T. Park, A. H. Zewail, Photon-induced near-field electron microscopy: Mathematical formulation of the relation between the experimental observables and the optically driven charge density of nanoparticles. *Phys Rev A* **89**, 013851 (2014).

37. R. Shiloh, Y. Lereah, Y. Lilach, A. Arie, Sculpturing the electron wave function using nanoscale phase masks. *Ultramicroscopy* **144**, 26–31 (2014).

38. D. Roitman, R. Shiloh, P. H. Lu, R. E. Dunin-Borkowski, A. Arie, Shaping of electron beams using sculpted thin films. *ACS Photonics* **8**, 3394–3405 (2021).

39. F. W. Olver, D. W. Lozier, R. F. Boisvert, C. W. Clark, *NIST Handbook of Mathematical Functions Hardback and CD-ROM* (Cambridge Univ. Press, 2010).

40. T. V. Teperik, A. Archambault, F. Marquier, J. J. Greffet, Huygens-Fresnel principle for surface plasmons. *Opt. Express* **17**, 17483–17490 (2009).

41. K. Zhang, W. Zuo, Y. Chen, D. Meng, L. Zhang, Beyond a Gaussian denoiser: Residual learning of deep CNN for image denoising. *IEEE Trans. Image Process.* **26**, 3142–3155 (2017).

42. Y. Shechtman, Y. C. Eldar, O. Cohen, H. N. Chapman, J. Miao, M. Segev, Phase retrieval with application to optical imaging: A contemporary overview. *IEEE Signal Process. Mag.* **32**, 87–109 (2015).

43. L. Taylor, The phase retrieval problem. *IEEE Trans. Antennas Propag.* **29**, 386–391 (1981).

44. Z. Wang, A. C. Bovik, H. R. Sheikh, E. P. Simoncelli, Image quality assessment: From error visibility to structural similarity. *IEEE Trans. Image Process.* **13**, 600–612 (2004).

45. Y. Wu, M. R. Ali, K. Chen, N. Fang, M. A. El-Sayed, Gold nanoparticles in biological optical imaging. *Nano Today* **24**, 120–140 (2019).

46. L. Novotny, N. van Hulst, Antennas for light. *Nat. Photonics* **5**, 83–90 (2011).

47. J. J. Storhoff, A. D. Lucas, V. Garimella, Y. P. Bao, U. R. Müller, Homogeneous detection of unamplified genomic DNA sequences based on colorimetric scatter of gold nanoparticle probes. *Nat. Biotechnol.* **22**, 883–887 (2004).

48. S. Sargazi, U. Laraib, S. Er, Application of green gold nanoparticles in cancer therapy and diagnosis. *Nanomaterials* **12**, 1102 (2022).

49. W. Qiang, W. Li, X. Li, X. Chen, D. Xu, Bioinspired polydopamine nanospheres: A super-quencher for fluorescence sensing of biomolecules. *Chem. Sci.* **5**, 3018–3024 (2014).

50. J. Reichert, A. Csáki, J. M. Köhler, W. Fritzsche, Chip-based optical detection of DNA hybridization by means of nanobead labeling. *Anal. Chem.* **72**, 6025–6029 (2000).

51. A. Csaki, P. Kaplanek, R. Moller, W. Fritzsche, The optical detection of individual DNA-conjugated gold nanoparticle labels after metal enhancement. *Nanotechnology* **14**, 1262–1268 (2003).

52. F. J. Garcia de Abajo, M. Kociak, Electron energy-gain spectroscopy. *New J. Phys.* **10**, 073035 (2008).

53. A. Karnieli, S. Tsesses, R. Yu, N. Rivera, Z. Zhao, A. Arie, S. Fan, I. Kaminer, Quantum sensing of strongly coupled light-matter systems using free electrons. *Sci. Adv.* **9**, eadd2349 (2023).

54. F. Houdellier, G. M. Caruso, S. Weber, M. J. Hÿtch, C. Gatel, A. Arbouet, Optimization of off-axis electron holography performed with femtosecond electron pulses. *Ultramicroscopy* **202**, 26–32 (2019).

55. R. Shiloh, T. Chlouba, P. Hommelhoff, Quantum-coherent light-electron interaction in a scanning electron microscope. *Phys. Rev. Lett.* **128**, 235301 (2022).

56. K. A. Taylor, R. M. Glaeser, Electron diffraction of frozen, hydrated protein crystals. *Science* **186**, 1036–1037 (1974).

57. M. Taleb, M. Hentschel, K. Rossnagel, H. Giessen, N. Talebi, Phase-locked photon–electron interaction without a laser. *Nat. Phys.* **19**, 869–876 (2023).

58. A. Gover, A. Yariv, Free-electron-bound-electron resonant interaction. *Phys. Rev. Lett.* **124**, 64801 (2020).

59. D. Nabben, J. Kuttruff, L. Stolz, A. Ryabov, P. Baum, Attosecond electron microscopy of sub-cycle optical dynamics. *Nature* **619**, 63–67 (2023).

60. T. Bucher, H. Nahari, H. Herzig Sheinfux, R. Ruimy, A. Niedermayr, R. Dahan, Q. Yan, Y. Adiv, M. Yannai, J. Chen, Y. Kurman, S. Tae Park, D. J. Masiel, E. Janzen, J. H. Edgar, F. Carbone, G. Bartal, S. Tsesses, F. H. L. Koppens, G. Maria Vanacore, I. Kaminer, Coherently amplified ultrafast imaging in a free-electron interferometer. arXiv:2305.04877 [physics.optics] (8 May 2023).

61. J. H. Gaida, H. Lourenco-Martins, M. Sivis, T. Rittmann, A. Feist, F. J Garcia de Abajo, C. Ropers, Attosecond electron microscopy by free-electron homodyne detection. arXiv:2305.03005 [physics.optics] (4 May 2023).